Singular value decomposition for photon-processing nuclear imaging systems and applications for reconstruction and computing null functions

Singular value decomposition for photon-processing nuclear imaging systems and applications for reconstruction and computing null functions

Abhinav K Jha[1]**, Harrison H Barrett**[2,3]**, Eric C Frey**[1]**,
Eric Clarkson**[2,3]**, Luca Caucci**[2] **and Matthew A Kupinski**[2,3]

[1] Division of Medical Imaging Physics, Department of Radiology, Johns Hopkins University, Baltimore, MD 21218, USA
[2] Center for Gamma Ray Imaging, Department of Medical Imaging, University of Arizona, Tucson, AZ 85721, USA
[3] College of Optical Sciences, University of Arizona, Tucson, AZ 85721, USA

E-mail: ajha4@jhmi.edu

Abstract

Recent advances in technology are enabling a new class of nuclear imaging systems consisting of detectors that use real-time maximum-likelihood (ML) methods to estimate the interaction position, deposited energy, and other attributes of each photon-interaction event and store these attributes in a list format. This class of systems, which we refer to as photon-processing (PP) nuclear imaging systems, can be described by a fundamentally different mathematical imaging operator that allows processing of the continuous-valued photon attributes on a per-photon basis. Unlike conventional photon-counting (PC) systems that bin the data into images, PP systems do not have any binning-related information loss. Mathematically, while PC systems have an infinite-dimensional null space due to dimensionality considerations, PP systems do not necessarily suffer from this issue. Therefore, PP systems have the potential to provide improved performance in comparison to PC systems. To study these advantages, we propose a framework to perform the singular-value decomposition (SVD) of the PP imaging operator. We use this framework to perform the SVD of operators that describe a general two-dimensional (2D) planar linear shift-invariant (LSIV) PP system and a hypothetical continuously rotating 2D single-photon emission computed tomography (SPECT) PP system. We then discuss two applications of the SVD framework. The first application is to decompose the object being imaged by the PP imaging system into measurement and null components. We

compare these components to the measurement and null components obtained with PC systems. In the process, we also present a procedure to compute the null functions for a PC system. The second application is designing analytical reconstruction algorithms for PP systems. The proposed analytical approach exploits the fact that PP systems acquire data in a continuous domain to estimate a continuous object function. The approach is parallelizable and implemented for graphics processing units (GPUs). Further, this approach leverages another important advantage of PP systems, namely the possibility to perform photon-by-photon real-time reconstruction. We demonstrate the application of the approach to perform reconstruction in a simulated 2D SPECT system. The results help to validate and demonstrate the utility of the proposed method and show that PP systems can help overcome the aliasing artifacts that are otherwise intrinsically present in PC systems.

(Some figures may appear in colour only in the online journal)

1. Introduction

In x-ray and gamma-ray imaging systems, the interaction of a photon with the detector can be described by multiple parameters. For example, consider a single-photon emission computed tomography (SPECT) system that consists of modular scintillation cameras where each camera has a monolithic scintillator and an array of photo-multiplier tubes (PMTs). In this system, for each detected gamma-ray photon, we could use the PMT outputs to estimate the three-dimensional (3D) coordinates of the position of interaction of the gamma-ray photon within the scintillator and the energy deposited at the interaction site. We could also estimate other information such as some measure of the shape of the region over which the energy is deposited, and parameters related to secondary site interactions. Finally, we could also record the time at which the interaction occurred. We refer to the parameters that describe the interaction event as the attributes (or attribute vector) of the detected photon.

One method of storing the photon attributes is to discretize the attribute space into multiple bins, and count and store the number of interaction events for which the attribute lies in the given bin. This leads to a binned image, also referred to as the projection or sinogram image in nuclear imaging systems, which is basically a multi-dimensional histogram of the number of selected events for which the attribute vector lies within a certain range. We refer to systems that store data in this binned image format as photon-counting (PC) systems. Imaging systems that consist of pixellated detectors and output the number of photons that are incident on each pixel also belong to the same category. These PC systems are described by a continuous-to-discrete (CD) operator (Barrett and Myers 2004, Madsen *et al* 2007, Peterson and Furenlid 2011, Taguchi and Iwanczyk 2013, Barrett *et al* 2014, 2015). In PC systems, the precise value of the attribute of each photon is lost due to the binning operation. For example, a photon-interaction event that deposits an energy of 124.3 keV at the interaction site could just be assigned to the energy window corresponding to energy values between, for example, 80–130 keV. This causes a loss in information about this photon attribute value, and two very different photons are treated similarly. Often in PC systems, many of the photon attributes are ignored, since storing them in the binned format requires considerable storage, and processing all these attributes using the PC system operator is complicated. Also, often many photon-interaction

events are discarded in the PC systems, such as those where the deposited energy lies below a certain value. Finally, there is a potential for information loss in the process of estimating the attributes.

These sources of information loss are avoided by another class of systems where, for each photon-interaction event, the measured sensor outputs are used to estimate the photon attributes using a real-time maximum-likelihood (ML) technique (Furenlid *et al* 2005, Barrett *et al* 2009, Hesterman *et al* 2010). As we will describe in section 2, it is important that the photon attributes are estimated using an ML technique to minimize the information loss in the estimation process. We then assume that all the attributes are stored at full precision in a list format. Thus, the data are defined over a continuous domain and there is no binning-related information loss. We refer to the stored data as list-mode (LM) data, although it must be noted that our use of the term list-mode goes beyond conventional usage, primarily because of storing multiple photon attributes, the ML estimation of these attributes and their storage at high precision. In contrast, conventionally, the list entry contains a simple pixel or centroid estimate for the position of interaction of the photon with the detector (Anger 1958, Barrett *et al* 2009, Peterson and Furenlid 2011). Finally, we process the stored photon attributes on a per-photon basis. We refer to these systems as photon-processing (PP) systems. Several such systems have been developed for nuclear imaging applications (Eskin 1997, Eskin *et al* 1998, Marks *et al* 1999, Furenlid *et al* 2004, Furenlid *et al* 2008, Miller *et al* 2008, Miller *et al* 2009a, 2009b, Moore *et al* 2012, Miller *et al* 2014).

The concept of PP systems, as opposed to PC systems, enables us to define an entirely new and fundamentally different mathematical model of imaging. This mathematical model for a nuclear imaging system is characterized by a linear continuous-to-continuous (CC) LM operator that maps from the space of object functions defined on a continuous domain to the space of LM data functions defined on another continuous domain. Further, this model allows extracting information from the individual continuous-valued photon attributes that have been estimated using an ML technique. An important mathematical difference between the PP and PC systems operators is that the latter maps from an infinite-dimensional Hilbert space to a finite-dimensional Euclidean space, and thus has an infinite-dimensional null space due to dimensionality considerations. Consequently, there is an infinite set of object components that cannot be measured by PC systems (Barrett *et al* 1991). The PP system operator does not necessarily suffer from this issue, as we will elaborate in section 3.1. Consequently, PP systems could provide improved performance in diagnostic and quantitative imaging tasks.

Investigating and quantifying the potential advantages that could be offered by PP systems requires the development of mathematical tools. An excellent tool for analyzing a linear imaging system, such as the PP nuclear imaging system, is singular value decomposition (SVD). SVD can be used to compute the null functions of a linear imaging systems, and thus characterize the object features that are not measured (Barrett *et al* 1991). Similarly, SVD can be used to design algorithms to reconstruct the object function (Gullberg and Zeng 1994, Barrett and Myers 2004). SVD can also be applied to assess image quality in terms of estimation tasks (Paxman *et al* 1985). Further, there is ongoing research on using the singular vectors as channels for mathematical observer models (Park *et al* 2009). In addition, SVD can also be used to investigate the noise properties in imaging systems (Kadrmas *et al* 1996). While SVD of tomographic systems has been a topic of active research (Davison and Grunbaum 1981, Aarsvold and Barrett 1996, Zeng and Gullberg 1997, Barrett and Myers 2004, Clarkson *et al* 2010), the SVD of the PP system operator has not been previously derived. In this paper, our primary objective is to derive the SVD of the system operator for PP nuclear imaging systems.

We also present the use of the derived SVD for two applications. The first application is to compute the null functions for PP systems and subsequently compare the null functions of PP and PC systems given an object function. Current methods to compute null functions for nuclear imaging systems approximate the system with a discrete-discrete (DD) operator (Zeng and Gullberg 1997, Wilson and Barrett 1998). This assumption leads to an inaccuracy in modeling the system and thus can lead to inaccurate and incomplete representation of the null functions. For example, the current methods compute a finite-dimensional null vector as opposed to a continuous null function. We exploit the CC nature of the LM operator to obtain continuous null functions, instead of finite-dimensional null vectors, for the PP system. The comparison of the null functions of PP and PC systems presents insights into the information loss that occurs due to the null space that is enforced by dimensionality considerations in PC systems. To perform this comparison appropriately, we designed an approach to obtain continuous null functions with PC systems.

The second presented application of the SVD framework is to design analytic reconstruction algorithms for PP systems. Analytic algorithms can leverage the true potential of PP systems due to their two inherent advantages: the ability to process data defined over a continuous domain to reconstruct continuous object functions and perform photon-by-photon reconstruction. While this is the first investigation to design algorithms for reconstructing object functions from PP systems, previously, methods have been developed to use LM data to reconstruct a discrete object vector (Parra and Barrett 1998, Bouwens *et al* 2001, Reader *et al* 2002, Khurd and Gindi 2004, Defrise *et al* 2005, Reader and Zaidi 2007, Schretter 2009). However, these methods implicitly assume that the object is voxelized. Since real objects are functions defined on a continuous domain, assumptions that restrict the object to a discrete vector lead to information loss, as we will detail in section 3.2. The analytic algorithm we derive overcomes these issues. Further, the algorithm offers several other advantages as discussed in section 6.

The paper is organized as follows. In section 2, the LM operator for a nuclear imaging system is defined and the framework for deriving the SVD of this operator is presented. The SVDs for 2D planar and 2D SPECT PP systems are derived. In section 3, we describe two applications of the proposed SVD framework: computing the null functions and designing analytic reconstruction methods. In section 4, we describe the methodology to simulate the PP system for the experiments and an implementation of the reconstruction algorithm on graphics processing units (GPUs). In section 5.1, we present and compare the measurement and null functions obtained with PP and PC systems for different phantom types, including a Shepp–Logan phantom. In section 5.2, the results with the reconstruction algorithm are presented and compared with reconstruction results obtained from PC systems. Finally, in section 6, we summarize the important conclusions of the paper and discuss the results.

2. SVD of PP systems

2.1. The PP system operator

Consider a PP nuclear imaging system imaging a radiotracer distribution. We will denote this radiotracer distribution by the scalar-valued function $f(\mathbf{r})$ where $\mathbf{r}$ is a vector with p components lying in $\mathbb{R}^p$ (usually $p = 2$ or 3). We assume that the function lies in the Hilbert space $\mathbb{L}_2(\mathbb{R}^p)$. This object is viewed over a measurement time τ by the imaging system, which detects the gamma-ray photons emitted by the object using a scintillation camera. In this analysis, we consider only scintillation cameras, but the theory developed here applies equally well to nuclear imaging systems with semiconductor detectors that use ML methods to estimate the

photon attributes (Eskin 1997, Eskin *et al* 1998, Marks *et al* 1999). For each detected photon, the photon attributes, such as the position of interaction of the photon with the detector and the energy deposited in the interaction event, are estimated using an ML technique. Let q denote the number of attributes estimated for each interaction event. For the jth event, the q attributes are grouped into a q-dimensional (q-D) vector, which we denote by $\hat{A}_j$. Let the number of detected events be denoted by J. The attributes $\hat{A}_j$ are statistically dependent and the number of events J is a Poisson-distributed random variable. Thus, the LM data consist of the set $\{\hat{A}_j, j = 1, 2 \dots J\}$ and the random variable J itself. The data can be described as a Poisson point process in attribute space $u(\hat{A})$ (Barrett *et al* 1997, Barrett and Myers 2004, Lehovich 2005, Caucci and Barrett 2012, Jha 2013) given by

$$u(\hat{A}) = \sum_{j=1}^{J} \delta(\hat{A} - \hat{A}_j), \tag{1}$$

where $\delta(\dots)$ denotes the q-D Dirac delta function. For the given object and a fixed acquisition time, taking the mean of the point process over J and $\hat{A}_j$ gives (Caucci and Barrett 2012)

$$\bar{u}(\hat{A}|f) = \int_{\mathbb{S}_f} \mathrm{d}^p r \ \tau \mathrm{pr}(\hat{A}|r)s(r)f(r), \tag{2}$$

where $\mathrm{pr}(\hat{A}|r)$ is the probability distribution function (PDF) for an event that originates with an emission at point r, $s(r)$ is the probability that an event that originated at point r in the object space will be detected and included in the list of events, and $\mathbb{S}_f$ denotes the support of the functions in object space. Further, let $\mathbb{S}_u$ denote the support of the functions in the LM data space. We assume that $\mathbb{S}_f \subset \mathbb{R}^p$ and $\mathbb{S}_u \subset \mathbb{R}^q$. Since the PP systems have finite object and data support, we also assume that the support sets are both compact sets, which therefore have finite p-dimensional and q-dimensional volume, respectively. Equation (2) can be written in operator form as

$$\bar{u}(\hat{A}|f) = [\mathcal{L}f](\hat{A}), \tag{3}$$

where $\mathcal{L}$ denotes the linear LM imaging operator (Lehovich 2005). Note that $\mathcal{L}$ is a linear operator even though the ML estimation step is non-linear. The kernel for the $\mathcal{L}$ operator is given by

$$l(\hat{A}, r) = \tau \mathrm{pr}(\hat{A}|r)s(r). \tag{4}$$

We now investigate whether the $\mathcal{L}$ operator is compact. The importance of compactness will become evident in section 2.2 when we propose the SVD framework. We note that $\mathcal{L}$ is an integral operator that maps from the Hilbert space $\mathbb{L}_2(\mathbb{S}_f)$ to $\mathbb{L}_2(\mathbb{S}_u)$, where both $\mathbb{S}_f$ and $\mathbb{S}_u$ are compact sets. According to the Hilbert–Schmidt condition, the operator will be compact if the kernel satisfies the following condition:

$$\int_{\mathbb{S}_u} \mathrm{d}^q \hat{A} \int_{\mathbb{S}_f} \mathrm{d}^p r \ |l(\hat{A}, r)|^2 < \infty. \tag{5}$$

Thus, if $l(\hat{A}, r) = \tau s(r)\mathrm{pr}(\hat{A}|r)$ satisfies this condition, the $\mathcal{L}$ operator is compact. One case where this condition will be satisfied is if $l(\hat{A}, r)$ is bounded (Halmos and Sunder 1978).

The kernel of the $\mathcal{L}$ operator can be rewritten by marginalizing equation (2) over the true attribute vector $\boldsymbol{A}$ as

$$l(\hat{\boldsymbol{A}}, \boldsymbol{r}) = \tau \int_{\mathbb{S}_u} \mathrm{d}^q A \, \mathrm{pr}(\hat{\boldsymbol{A}}|\boldsymbol{A})\mathrm{pr}(\boldsymbol{A}|\boldsymbol{r})s(\boldsymbol{r}). \tag{6}$$

Since the function $s(\boldsymbol{r})$ is the probability that an event that originated at point $\boldsymbol{r}$ in the object space is detected and included in the list of events, $s(\boldsymbol{r}) \leqslant 1$ for all $\boldsymbol{r}$.

The attribute vector $\hat{\boldsymbol{A}}$ is estimated optimally using an ML estimation technique. The ML estimator is efficient, i.e. it is unbiased and attains the Cramér-Rao lower bound (CRLB), if an efficient estimator exists. Further, ML estimates are asymptotically efficient and consistent under most conditions (Barrett and Myers 2004). This asymptotic limit is closely approached in scintillation cameras because for each detected gamma-ray photon, a large number of optical photons are emitted and used to estimate the photon attributes (Barrett *et al* 2009, Caucci *et al* 2010, Bora *et al* 2015). Moreover, in this asymptotic limit, the ML estimates have a multivariate normal distribution with mean equal to the true attribute value, and the covariance matrix of the estimates is the inverse of the Fisher information matrix $\boldsymbol{F}(\boldsymbol{A})$ for estimating $\hat{\boldsymbol{A}}$ from the PMT signals, i.e.

$$\mathrm{pr}(\hat{\boldsymbol{A}}|\boldsymbol{A}) = \frac{\sqrt{|\boldsymbol{F}(\boldsymbol{A})|}}{[2\pi]^{q/2}} \exp\left[-\frac{1}{2}(\hat{\boldsymbol{A}} - \boldsymbol{A})^\dagger \boldsymbol{F}(\boldsymbol{A})(\hat{\boldsymbol{A}} - \boldsymbol{A})\right], \tag{7}$$

where $|\boldsymbol{F}(\boldsymbol{A})|$ denotes the determinant of the Fisher information matrix.

2.2. General framework for SVD of PP system operator

Let $\mathcal{L}^\dagger$ denote the adjoint (backprojection operator) of the LM imaging operator $\mathcal{L}$. A convenient way to derive the SVD of the $\mathcal{L}$ operator is to start by solving the eigenvalue equations for $\mathcal{L}^\dagger\mathcal{L}$ or $\mathcal{L}\mathcal{L}^\dagger$ operators (Barrett and Myers 2004). Since the $\mathcal{L}$ operator is compact, the eigenvalue equation for $\mathcal{L}^\dagger\mathcal{L}$ is given by

$$[\mathcal{L}^\dagger\mathcal{L}w_n](\boldsymbol{r}) = \mu_n w_n(\boldsymbol{r}), \quad n = 1, \ldots, \infty \tag{8}$$

where $w_n(\boldsymbol{r})$ and μ_n denotes the eigenfunctions and eigenvalues of the $\mathcal{L}^\dagger\mathcal{L}$ operator and n denotes the index for these eigenfunctions or eigenvalues (Barrett and Myers 2004). In this paper, we often denote vectors by boldface type. Further, we consider functions to be associated with vectors in the Hilbert space. For example, $w_n(\boldsymbol{r})$ is considered to be associated with $\boldsymbol{w}_n$. The operator $\mathcal{L}^\dagger\mathcal{L}$ maps from $\mathbb{L}_2(\mathbb{S}_f)$ to $\mathbb{L}_2(\mathbb{S}_f)$. Further, $\mathcal{L}^\dagger\mathcal{L}$ is a Hermitian and nonnegative-definite operator, so that the eigenvalues μ_n are real and nonnegative (Barrett and Myers 2004).

The eigenvalues for the $\mathcal{L}\mathcal{L}^\dagger$ operator are the same as for the $\mathcal{L}^\dagger\mathcal{L}$ operator. The eigenvalue equation for $\mathcal{L}\mathcal{L}^\dagger$ is given by

$$[\mathcal{L}\mathcal{L}^\dagger v_n](\hat{\boldsymbol{A}}) = \mu_n v_n(\hat{\boldsymbol{A}}), \quad n = 1, \ldots, \infty, \tag{9}$$

where $v_n(\hat{\boldsymbol{A}})$ denotes the eigenfunctions of the $\mathcal{L}\mathcal{L}^\dagger$ operator. These eigenfunctions can also be obtained from $\boldsymbol{w}_n$ using the equation

$$v_n(\hat{\boldsymbol{A}}) = \frac{1}{\sqrt{\mu_n}}[\mathcal{L}w_n](\hat{\boldsymbol{A}}), \tag{10}$$

provided w_n is not a null vector. Having obtained these eigenvalues and eigenvectors, the singular values, object-space singular functions and data-space singular functions for the $\mathcal{L}$ operator are simply given by $\sqrt{\mu_n}$, w_n, and v_n, respectively. The SVD representation of the $\mathcal{L}$ operator, as defined by its action on a function such as $f(r)$, is given by

$$[\mathcal{L}f](\hat{A}) = \sum_{n=1}^{\infty} \sqrt{\mu_n}(w_n, f)v_n, \tag{11}$$

where (w_n, f) denotes the scalar product of the vectors w_n and f, and is defined as

$$(w_n, f) = \int_{\mathbb{S}_f} \mathrm{d}^q r \ w_n^*(r)f(r). \tag{12}$$

where $w_n^*(r)$ denotes the complex conjugate of $w_n(r)$.

In the examples in this paper, to derive the SVD of the $\mathcal{L}$ operator, we will perform the eigenanalysis of the $\mathcal{L}^\dagger\mathcal{L}$ operator. Using equation (4) and the definition of the adjoint (Barrett and Myers 2004), we can show that the expression for the $\mathcal{L}^\dagger$ operator is given by

$$[\mathcal{L}^\dagger \overline{u}](r) = \tau \int_{\mathbb{S}_u} \mathrm{d}^q \hat{A} \ \mathrm{pr}(\hat{A}|r)s(r)\bar{u}(\hat{A}). \tag{13}$$

With equations (4) and (13), the expression for the $\mathcal{L}^\dagger\mathcal{L}$ operator is given by

$$[\mathcal{L}^\dagger\mathcal{L}f](r') = \tau^2 \int_{\mathbb{S}_u} \mathrm{d}^q \hat{A} \int_{\mathbb{S}_f} \mathrm{d}^p r \ s(r)s(r')\mathrm{pr}(\hat{A}|r')\mathrm{pr}(\hat{A}|r)f(r). \tag{14}$$

Therefore, the kernel for $\mathcal{L}^\dagger\mathcal{L}$ operator, which we denote by $k(r', r)$, is given by

$$k(r', r) = \tau^2 \int_{\mathbb{S}_u} \mathrm{d}^q \hat{A} \ s(r)s(r')\mathrm{pr}(\hat{A}|r)\mathrm{pr}(\hat{A}|r'). \tag{15}$$

We thus have a general framework that we can apply to specific PP imaging systems to perform their SVD.

The framework proposed in this section has been developed for realistic PP systems, and thus it is assumed that the systems have finite object and data support. However, in the specific analytical examples that we next consider, the systems will be assumed to have infinite object and data support. This assumption is made mainly for mathematical convenience. Making this assumption requires considering an analogous version of the proposed framework for a class of non-compact operators.

The applications of the SVD framework presented in this paper will require deriving the pseudoinverse of the $\mathcal{L}$ operator. This pseudoinverse, which we denote by $\mathcal{L}^+$, can be determined from the singular values and the singular vectors of the $\mathcal{L}$ operator (Barrett and Myers 2004). The action of the $\mathcal{L}^+$ operator on a function in the data space, such as $\bar{u}(\hat{A})$, is given by

$$[\mathcal{L}^+\bar{u}](r) = \sum_{n=1}^{\infty} \frac{1}{\sqrt{\mu_n}}(v_n, \bar{u})w_n. \tag{16}$$

2.3. A 2D planar LSIV PP system

Let us consider a planar 2D LSIV PP imaging system that images a 2D object, $f(r)$, using a planar 2D detector. This system approximates a planar nuclear imaging system that images a planar gamma-ray source using a fine-bore parallel-hole collimator onto a scintillation

camera. The camera uses a PMT array to sense the scintillation light, where the output of the PMT array is used to estimate the 2D position of interaction of the gamma-ray photon with the scintillator using a ML technique. Further, it is assumed that the resolution blur introduced due to the collimator is negligible compared to the estimation blur. Finally, since this is a LSIV system, it has infinite object and data support.

In this planar system, the photon attributes are the *x* and *y* coordinates of the detected event. Let us denote the true and estimated values of these attributes by the 2D vectors $\boldsymbol{R}$ and $\hat{\boldsymbol{R}}$, respectively. The LM data can be described by the point process $u(\hat{\boldsymbol{R}})$:

$$u(\hat{\boldsymbol{R}}) = \sum_{j=1}^{J} \delta(\hat{\boldsymbol{R}} - \hat{\boldsymbol{R}}_j). \tag{17}$$

The model for this planar LSIV system is given by

$$\bar{u}(\hat{\boldsymbol{R}}) = \int_{\infty} \mathrm{d}^2 r \, f(\boldsymbol{r}) l(\hat{\boldsymbol{R}}, r) = [\mathcal{L}f](\hat{\boldsymbol{R}}). \tag{18}$$

where the subscript ∞ on the integral sign denotes an integral over the infinite object support. To derive the expression for the $\mathcal{L}$ operator, in accordance with equation (4), we must determine the expression for $\mathrm{pr}(\hat{\boldsymbol{R}}|r)$. Since the system is LSIV, the normalized point spread function (PSF) of the imaging system, $h(\boldsymbol{R}, r)$ can be written as $h(\boldsymbol{R} - r)$, so that

$$\mathrm{pr}(\boldsymbol{R}|r) = h(\boldsymbol{R} - r). \tag{19}$$

We also assume that $s(\boldsymbol{r})$ is equal to unity for all $\boldsymbol{r}$ and that a large number of photons were used to estimate the attributes. Then, using equation (7) and further, assuming that the Fisher information matrix corresponding to the estimate of $\hat{\boldsymbol{R}}$ is independent of $\boldsymbol{R}$, we can write

$$\mathrm{pr}(\hat{\boldsymbol{R}}|\boldsymbol{R}) = \frac{\sqrt{|F|}}{2\pi} \exp\left[-\frac{1}{2}(\hat{\boldsymbol{R}} - \boldsymbol{R})^{\dagger} F(\hat{\boldsymbol{R}} - \boldsymbol{R}) \right]. \tag{20}$$

We denote $\mathrm{pr}(\hat{\boldsymbol{R}}|\boldsymbol{R})$ by $\gamma(\hat{\boldsymbol{R}} - \boldsymbol{R})$, where this simplified expression recognizes the fact that $\mathrm{pr}(\hat{\boldsymbol{R}}|\boldsymbol{R})$ is a function of $\hat{\boldsymbol{R}} - \boldsymbol{R}$. Substituting the expressions from equations (19) and (20) in the equation analogous to equation (6) for this system, we get

$$l(\hat{\boldsymbol{R}}, r) = \tau \int_{\infty} \mathrm{d}^2 R \, h(\boldsymbol{R} - r) \gamma(\hat{\boldsymbol{R}} - \boldsymbol{R})$$

$$= \tau \int_{\infty} \mathrm{d}^2 R' \, h(\boldsymbol{R}') \gamma(\hat{\boldsymbol{R}} - r - \boldsymbol{R}'), \tag{21}$$

where in the second step, we have performed a change of variables by replacing $\boldsymbol{R} - r$ by $\boldsymbol{R}'$. We recognize that, given the infinite object support, this is a convolution operation, so we can write

$$l(\hat{\boldsymbol{R}}, r) = \tau[h * \gamma](\hat{\boldsymbol{R}} - r), \tag{22}$$

where $[f * g](x)$ denotes the convolution of functions $f(x)$ and $g(x)$. Since the kernel for the $\mathcal{L}$ operator is a function of $\hat{\boldsymbol{R}} - r$, $\mathcal{L}$ resembles a convolution operator. This operator is not compact and its eigen values form a continuous spectrum. The eigenvalue equation for this operator can be written as

$$\mathcal{L}\phi_{\rho} = \lambda_{\rho}\phi_{\rho}, \tag{23}$$

where $\boldsymbol{\rho}$ denotes a continuous 2D index. However, even though the $\mathcal{L}$ operator is not compact, since it is a convolution operator, Fourier theory provides a convenient way to perform the SVD of this operator. It can be shown that the eigenfunctions of $\mathcal{L}$ are the complex exponentials (Barrett and Myers 2004)

$$\phi_{\rho}(\boldsymbol{r}) = \exp(2\pi i\boldsymbol{\rho} \cdot \boldsymbol{r}). \tag{24}$$

We can show that the corresponding eigenvalues are given by the Fourier transform of the kernel of the $\mathcal{L}$ operator, i.e.

$$\lambda_{\rho} = [\mathcal{F}_2 l](\boldsymbol{\rho}) = \tau H(\boldsymbol{\rho})\Gamma(\boldsymbol{\rho}), \tag{25}$$

where $\mathcal{F}_2$ denotes the 2D Fourier transform operator, so that $\mathcal{F}_2\{h(\boldsymbol{r})\} = H(\boldsymbol{\rho})$ and $\mathcal{F}_2\{\gamma(\boldsymbol{r})\} = \Gamma(\boldsymbol{\rho})$. In the second step, we substitute the expression for $l(\hat{\boldsymbol{R}}, \boldsymbol{r})$ from equation (22) and then invoke the convolution theorem. By taking the Fourier transform of the function $\gamma(\boldsymbol{r})$ (equation (20)), we can show that the expression for $\Gamma(\boldsymbol{\rho})$ is given by (Barrett and Myers 2004)

$$\Gamma(\boldsymbol{\rho}) = \exp(-2\pi^2 \boldsymbol{\rho}^{\dagger} \boldsymbol{F}^{-1} \boldsymbol{\rho}), \tag{26}$$

where $\boldsymbol{F}$ is the 2×2 Fisher information matrix. Since $\mathcal{L}$ is a convolution operator, its adjoint is also a convolution operation, with a kernel given by $l^*(\boldsymbol{r}, \hat{\boldsymbol{R}})$, where $*$ denotes the complex conjugate. We can easily show that (Barrett and Myers 2004)

$$\mathcal{L}^{\dagger}\phi_{\rho} = \lambda_{\rho}^*\phi_{\rho}. \tag{27}$$

Using equations (23) and (27), we obtain

$$[\mathcal{L}^{\dagger}\mathcal{L}\phi_{\rho}](\boldsymbol{r}) = |\lambda_{\rho}|^2\phi_{\rho}(\boldsymbol{r}). \tag{28}$$

Thus, the eigenfunctions and eigenvalues of $\mathcal{L}^{\dagger}\mathcal{L}$ are the complex exponentials $\phi_{\rho}(\boldsymbol{r})$ and $|\lambda_{\rho}|^2$, respectively. By analogy to equation (8), the object-space singular functions, which we denote by $w_{\rho}(\boldsymbol{r})$, are equal to $\phi_{\rho}(\boldsymbol{r})$, so that

$$w_{\rho}(\boldsymbol{r}) = \exp(2\pi i\boldsymbol{\rho} \cdot \boldsymbol{r}), \tag{29}$$

and the corresponding singular values for these singular functions are

$$\sqrt{\mu_{\rho}} = |\lambda_{\rho}| = \tau|H(\boldsymbol{\rho})|\Gamma(\boldsymbol{\rho}). \tag{30}$$

Inserting the expressions from equation (29) and (30) into equation (10), we obtain the expression for the singular functions in image space as

$$v_{\rho}(\hat{\boldsymbol{R}}) = \frac{1}{\sqrt{\mu_{\rho}}}[\mathcal{L}w_{\rho}](\hat{\boldsymbol{R}}) = \frac{H(\boldsymbol{\rho})}{|H(\boldsymbol{\rho})|}\exp(2\pi i\boldsymbol{\rho} \cdot \hat{\boldsymbol{R}}). \tag{31}$$

Thus, using equations (29)–(31), we obtain the singular values and singular functions for this imaging system. To derive the pseudoinverse for this operator, we substitute the expressions from equations (29)–(31) in the continuous analog of equation (16). This yields

$$[\mathcal{L}^+\overline{u}](\boldsymbol{r}) = \frac{1}{\tau}\int_{\infty} d^2\rho \frac{1}{H(\boldsymbol{\rho})}\exp(2\pi^2\boldsymbol{\rho}^{\dagger}\boldsymbol{F}^{-1}\boldsymbol{\rho})\exp\{2\pi i\boldsymbol{\rho} \cdot (\boldsymbol{r} - \hat{\boldsymbol{R}})\}\overline{u}(\hat{\boldsymbol{R}}), \tag{32}$$
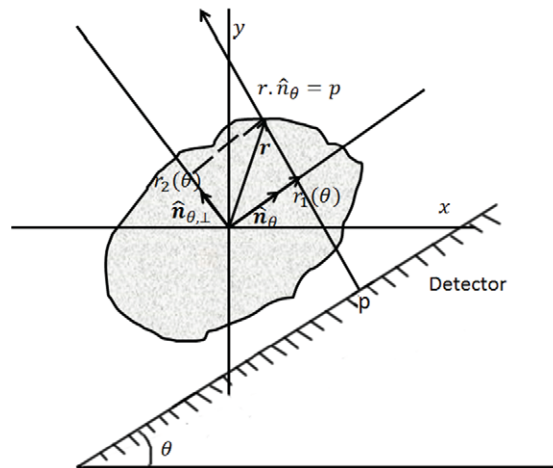
Figure 1. A schematic illustrating the various mathematical notations for the considered 2D SPECT system.

where we have inserted the expression for $\Gamma(\boldsymbol{\rho})$ from equation (26). Note that equations (31) and (32) are only applicable for $\boldsymbol{\rho}$ values where $H(\boldsymbol{\rho}) \neq 0$. An easy way to overcome this limitation is by replacing $H(\boldsymbol{\rho})$ by $H(\boldsymbol{\rho}) + \epsilon$, where ϵ is a very small number.

2.4. A 2D tomographic PP imaging system

Consider a continuously rotating 2D SPECT imaging system with an infinite object support where the object and photon propagation is in the *x–y* plane, as shown in figure 1. The SPECT imaging system consists of a parallel-hole collimator with holes on a regular grid, followed by a 1D detector. The system continuously rotates about the *z* axis over an angular range of π radians, acquiring data at angles θ, where θ denotes the angle that the detector makes with the *x*-axis. We assume that the parallel-hole collimator accepts photons only normal to the detector surface. Also, we ignore attenuation and scatter in this analysis. Finally, it is also assumed that both the object and data support are infinite. For each LM event, the coordinate of the position of interaction of the gamma-ray photon with the scintillation crystal is estimated and recorded. We denote the estimated position of interaction by $\hat{p}$, and its corresponding true value by p. The angular orientation of the detector, θ, is also recorded. Thus, the *j*th attribute vector for this system is given by $\hat{A}_j = (\hat{p}_j, \theta_j)$, and the LM process corresponding to the data acquired by this system is given by

$$u(\hat{p}, \theta) = \sum_{j=1}^{J} \delta(\hat{p} - \hat{p}_j)\delta(\theta - \theta_j). \tag{33}$$

The mathematical description for this imaging system is given by

$$\bar{u}(\hat{p}, \theta) = \int_{\infty} \mathrm{d}^2 r\, f(\boldsymbol{r}) l(\hat{p}, \theta, \boldsymbol{r}) = \mathcal{L}f. \tag{34}$$

To derive the expression for the $\mathcal{L}$ operator for this system, in accordance with equation (4), we have to determine the expression for $\mathrm{pr}(\hat{p}, \theta | \boldsymbol{r})$. Using marginal probabilities, we can write

$$\mathrm{pr}(\hat{p}, \theta \mid \boldsymbol{r}) = \mathrm{pr}(\theta \mid \boldsymbol{r}) \int_{-\infty}^{\infty} \mathrm{d}p \ \mathrm{pr}(\hat{p} \mid p, \theta, \boldsymbol{r}) \mathrm{pr}(p \mid \theta, \boldsymbol{r}). \tag{35}$$

The probability of the position of interaction p given a particular value of the detector angle θ and object location $\boldsymbol{r}$ is simply the delta function $\delta(p - \boldsymbol{r} \cdot \hat{\boldsymbol{n}}_\theta)$, where $\hat{\boldsymbol{n}}_\theta$ is the unit vector parallel to the detector face when the detector is aligned at the angle θ. Thus

$$\mathrm{pr}(p \mid \theta, \boldsymbol{r}) = \delta(p - \boldsymbol{r} \cdot \hat{\boldsymbol{n}}_\theta). \tag{36}$$

The attribute $\hat{p}$ is estimated with an ML approach using a large number of scintillation photons. Thus, using equation (7), and denoting the CRLB on the estimate of p by σ_p^2, we can write

$$\mathrm{pr}(\hat{p} \mid p, \theta, \boldsymbol{r}) = \mathrm{pr}(\hat{p} \mid p) = \frac{1}{\sqrt{2\pi}\,\sigma_p} \exp\left[-\frac{(\hat{p} - p)^2}{2\sigma_p^2}\right]. \tag{37}$$

Further, due to the isotropic emission of photons, the angle of emission of photons is a uniformly distributed random variable. Since the detector rotates with uniform angular velocity over a range of π radians, when a photon is detected, the recorded angular orientation of the detector θ will also be uniformly distributed between 0 and π radians. Thus,

$$\mathrm{pr}(\theta \mid \boldsymbol{r}) = \mathrm{pr}(\theta) = \frac{1}{\pi} 1_{[0,\pi]}(\theta). \tag{38}$$

where $1_{[\alpha,\beta]}(\theta)$ denotes the indicator function, and is defined as follows:

$$1_{[\alpha,\beta]}(\theta) = \begin{cases} 1 & \text{if } \alpha \leqslant \theta \leqslant \beta. \\ 0 & \text{otherwise.} \end{cases} \tag{39}$$

Under the assumption that $s(\boldsymbol{r})$ is unity for all values of $\boldsymbol{r}$, using equations (4), (35)–(38), we can show that the kernel of the LM operator $\mathcal{L}$ is given by

$$l(\hat{p}, \theta, \boldsymbol{r}) = \frac{\tau}{\pi} \frac{1}{\sqrt{2\pi}\,\sigma_p} \exp\left[-\frac{(\hat{p} - \boldsymbol{r} \cdot \hat{\boldsymbol{n}}_\theta)^2}{2\sigma_p^2}\right] 1_{[0,\pi]}(\theta). \tag{40}$$

Therefore, using equation (15), we can show that the kernel $k(\boldsymbol{r}', \boldsymbol{r})$ for the $\mathcal{L}^\dagger \mathcal{L}$ operator is given by

$$k(\boldsymbol{r}', \boldsymbol{r}) = \left[\frac{\tau}{\pi}\right]^2 \frac{1}{2\pi\sigma_p^2} \int_{-\infty}^{\infty} \mathrm{d}\hat{p} \int_0^\pi \mathrm{d}\theta \exp\left[-\frac{(\hat{p} - \boldsymbol{r}' \cdot \hat{\boldsymbol{n}}_\theta)^2}{2\sigma_p^2} - \frac{(\hat{p} - \boldsymbol{r} \cdot \hat{\boldsymbol{n}}_\theta)^2}{2\sigma_p^2}\right]. \tag{41}$$

We perform a change of variables by replacing $\hat{p} - \boldsymbol{r} \cdot \hat{\boldsymbol{n}}_\theta$ by q. Simplifying further, we obtain

$$k(\boldsymbol{r}', \boldsymbol{r}) = \left[\frac{\tau}{\pi}\right]^2 \frac{1}{2\pi\sigma_p^2} \int_0^\pi \mathrm{d}\theta \exp\left[\frac{\{-(\boldsymbol{r} - \boldsymbol{r}') \cdot \hat{\boldsymbol{n}}_\theta\}^2}{4\sigma_p^2}\right] \int_{-\infty}^{\infty} \mathrm{d}q \exp\left[-\frac{\left\{q - \frac{(\boldsymbol{r} - \boldsymbol{r}') \cdot \hat{\boldsymbol{n}}_\theta}{2}\right\}^2}{\sigma_p^2}\right]. \tag{42}$$

Evaluating the integral over q yields

$$k(\mathbf{r}', \mathbf{r}) = \left[\frac{\tau}{\pi}\right]^2 \frac{1}{\sqrt{2\pi}\,\sigma_p} \int_0^\pi d\theta \exp\left[\frac{-\{(\mathbf{r} - \mathbf{r}') \cdot \hat{\mathbf{n}}_\theta\}^2}{4\sigma_p^2}\right]. \tag{43}$$

We see that $k(\mathbf{r}', \mathbf{r})$, which is the kernel of the $\mathcal{L}^\dagger\mathcal{L}$ operator, is a function of $\mathbf{r} - \mathbf{r}'$, so that we can define $\tilde{k}(\mathbf{r} - \mathbf{r}') = k(\mathbf{r}, \mathbf{r}')$. Thus, with the system having an infinite object and data support, $\mathcal{L}^\dagger\mathcal{L}$ resembles a convolution operator and the eigenanalysis of this operator can be performed via Fourier analysis. The eigenfunctions of $\mathcal{L}^\dagger\mathcal{L}$ are the complex exponentials given by

$$w_\rho(\mathbf{r}) = \exp(2\pi i \boldsymbol{\rho} \cdot \mathbf{r}). \tag{44}$$

The corresponding eigenvalues for these eigenfunctions are determined by computing the Fourier transform of the convolution kernel of the $\mathcal{L}^\dagger\mathcal{L}$ operator (equation (43)). Denoting the Fourier transform of $\tilde{k}(\mathbf{r} - \mathbf{r}')$ at frequency $\boldsymbol{\rho}$ by $K(\boldsymbol{\rho})$, we obtain

$$K(\boldsymbol{\rho}) = \left[\frac{\tau}{\pi}\right]^2 \frac{1}{\sqrt{2\pi}\,\sigma_p} \int_0^\pi d\theta \int_\infty d^2\mathbf{r} \exp\left[\frac{-(\mathbf{r} \cdot \hat{\mathbf{n}}_\theta)^2}{4\sigma_p^2}\right] \exp(-2\pi i\,\boldsymbol{\rho} \cdot \mathbf{r}). \tag{45}$$

Let the unit vector perpendicular to $\hat{\mathbf{n}}_\theta$ be denoted by $\hat{\mathbf{n}}_{\perp,\theta}$, as shown in figure 1. Expressing the vectors $\mathbf{r}$ and $\boldsymbol{\rho}$ in terms of the basis vectors $\hat{\mathbf{n}}_\theta$ and $\hat{\mathbf{n}}_{\perp,\theta}$ as $\mathbf{r} = r_1(\theta)\hat{\mathbf{n}}_\theta + r_2(\theta)\hat{\mathbf{n}}_{\perp,\theta}$ and $\boldsymbol{\rho} = \rho_1(\theta)\hat{\mathbf{n}}_\theta + \rho_2(\theta)\hat{\mathbf{n}}_{\perp,\theta}$, respectively, we can rewrite the above equation as

$$K(\boldsymbol{\rho}) = \left[\frac{\tau}{\pi}\right]^2 \frac{1}{\sqrt{2\pi}\,\sigma_p}$$

$$\times \int_0^\pi d\theta \int_{-\infty}^\infty dr_1(\theta) \exp\left[-\frac{r_1^2(\theta)}{4\sigma_p^2}\right] \exp[-2\pi i\rho_1(\theta)r_1(\theta)] \int_{-\infty}^\infty dr_2(\theta) \exp[-2\pi i\rho_2(\theta)r_2(\theta)]$$

$$= \left[\frac{\tau}{\pi}\right]^2 \int_0^\pi d\theta \exp[-4\pi^2\sigma_p^2\rho_1^2(\theta)]\delta[\rho_2(\theta)]. \tag{46}$$

To evaluate the integral over θ, we first express the vector $\boldsymbol{\rho}(\mathbf{r})$ in terms of its polar coordinates as $(|\boldsymbol{\rho}|, \varphi_\rho)$. The angle between $\hat{\mathbf{n}}$ and $\boldsymbol{\rho}$ is thus $\theta - \varphi_\rho$, so that

$$\rho_1(\theta) = |\boldsymbol{\rho}|\cos(\theta - \varphi_\rho), \tag{47a}$$

$$\rho_2(\theta) = |\boldsymbol{\rho}|\sin(\theta - \varphi_\rho). \tag{47b}$$

We note that the argument of the delta function $\delta(\rho_2(\theta))$ in equation (46) is itself another function. Consider a function $\delta[g(x)]$, where $g(x)$ is a function that vanishes at $x = x_n, n = 1, 2, \ldots N$. This function can be written as (Barrett and Myers 2004)

$$\delta[g(x)] = \sum_{n=1}^N \frac{\delta(x - x_n)}{|g'(x_n)|}, \tag{48}$$

where $g'(x_n)$ denotes the derivative of the function $g(x)$ evaluated at $x = x_n$. From equation (47b), we see that the function $\rho_2(\theta)$ vanishes when $\theta = \varphi_\rho$, i.e. when $\boldsymbol{\rho}$ is parallel to $\hat{\mathbf{n}}_\theta$. Thus, using the identity in equation (48), $\delta[\rho_2(\theta)]$ can be written as

$$\delta[\rho_2(\theta)] = \delta[|\boldsymbol{\rho}|\sin(\theta - \varphi_\rho)] = \frac{\delta(\theta - \varphi_\rho)}{|\boldsymbol{\rho}|} \tag{49}$$

Substituting this expression and the expression for $\rho_1(\theta)$ from equation (47) in equation (46), we obtain

$$
\begin{aligned}
K(\boldsymbol{\rho}) &= \left[\frac{\tau}{\pi}\right]^2 \int_0^\pi \mathrm{d}\theta \exp[-4\pi^2\sigma_p^2|\boldsymbol{\rho}|^2\cos^2(\theta - \phi_\rho)] \frac{\delta(\theta - \varphi_\rho)}{|\boldsymbol{\rho}|} \\
&= \frac{1}{|\rho|}\left[\frac{\tau}{\pi}\right]^2 \exp(-4\pi^2\sigma_p^2\rho^2)
\end{aligned} \tag{50}
$$

where we have used the sifting property of the delta function. Also, we have defined ρ such that $\boldsymbol{\rho} = |\rho|\hat{\boldsymbol{n}}_\theta$, where the absolute value sign is needed if we allow ρ to be signed, so that $\rho = \pm|\boldsymbol{\rho}|$. Using equation (10), we can show that the singular vectors for the $\mathcal{L}$ operator in data space are given by

$$
\begin{aligned}
v_\rho(\hat{p}, \theta) &= \frac{1}{\sqrt{K(\boldsymbol{\rho})}}[\mathcal{L}w_\rho](\hat{p}, \theta) \\
&= \exp(2\pi^2\sigma_p^2\rho^2)\sqrt{|\rho|} \int_\infty \mathrm{d}^2\boldsymbol{r}\frac{1}{\sqrt{2\pi}\,\sigma_p}\exp\left[-\frac{(\hat{p} - \boldsymbol{r}\cdot\hat{\boldsymbol{n}}_\theta)^2}{2\sigma_p^2}\right]\exp(2\pi\mathrm{i}\boldsymbol{\rho}\cdot\boldsymbol{r}),
\end{aligned} \tag{51}
$$

where we have used equations (34), (40), (44) and (50) to evaluate $[\mathcal{L}w](\hat{p}, \theta)$. Expressing the vectors $\boldsymbol{r}$ and $\boldsymbol{\rho}$ in terms of the basis vectors $\hat{\boldsymbol{n}}_\theta$ and $\hat{\boldsymbol{n}}_{\perp,\theta}$ as previously, and simplifying the resulting expression, we obtain

$$v_\rho(\hat{p}, \theta) = \sqrt{|\rho|}\,\exp[2\pi\mathrm{i}\hat{p}\rho_1(\theta)]\exp[2\pi^2\sigma_p^2\{\rho^2 - \rho_1^2(\theta)\}]\delta[\rho_2(\theta)]. \tag{52}$$

We thus obtain the SVD of the $\mathcal{L}$ operator for this system. To compute the pseudoinverse, we substitute the expressions obtained in equations (44), (50) and (52) in the continuous analog of equation (16). This yields

$$
\begin{aligned}
[\mathcal{L}^+&\overline{u}](\boldsymbol{r}) \\
&= \frac{\pi}{\tau}\int_{-\infty}^\infty \mathrm{d}^2\boldsymbol{\rho}\,\exp(2\pi\mathrm{i}\boldsymbol{\rho}\cdot\boldsymbol{r})|\rho|\exp[2\pi^2\sigma_p^2\{2\rho^2 - \rho_1^2(\theta)\}]\exp[-2\pi\mathrm{i}\hat{p}\rho_1(\theta)]\delta[\rho_2(\theta)]\overline{u}(\hat{A}) \\
&= \frac{\pi}{\tau}\int_{-\infty}^\infty \mathrm{d}\rho_1(\theta)\exp[2\pi\mathrm{i}\rho_1(\theta)r_1(\theta)]\exp[-2\pi\mathrm{i}\hat{p}\rho_1(\theta)] \\
&\quad\times \int_{-\infty}^\infty \mathrm{d}\rho_2(\theta)|\rho|\exp[2\pi^2\sigma_p^2\{2\rho^2 - \rho_1^2(\theta)\}]\delta[\rho_2(\theta)]\overline{u}(\hat{A}) \\
&= \frac{\pi}{\tau}\int_{-\infty}^\infty \mathrm{d}\rho\,|\rho|\exp[2\pi\mathrm{i}\rho\{r_1(\theta) - \hat{p}\}]\exp(2\pi^2\sigma_p^2\rho^2)\overline{u}(\hat{A}).
\end{aligned} \tag{53}
$$

where in the third step, we have used the sifting property of the delta function and the fact that the function $\delta_2(\theta)$ vanishes when $\boldsymbol{\rho}$ is parallel to $\hat{\boldsymbol{n}}_\theta$.

3. Applications of the SVD framework

3.1. Computing the null functions

Given a linear imaging system, such as the PC nuclear imaging system (characterized by the system operator $\mathcal{H}$), any object function $f(\boldsymbol{r})$ being imaged through this system can be decomposed into two orthogonal components, $f_{\text{meas}}(\boldsymbol{r})$ and $f_{\text{null}}(\boldsymbol{r})$, such that

$$f(\boldsymbol{r}) = f_{\text{meas}}(\boldsymbol{r}) + f_{\text{null}}(\boldsymbol{r}) \tag{54}$$

and

$$\mathcal{H}f_{\text{null}}(\boldsymbol{r}) = \mathbf{0}. \tag{55}$$

Thus, when an object $f(\boldsymbol{r})$ is imaged through a linear imaging system, the null component $f_{\text{null}}(\boldsymbol{r})$ is not imaged, and cannot be retrieved even from the noise-free data. Any object consisting of only these null components will be invisible to the system, and is termed a null function, invisible object, or ghost object of the imaging system (Barrett *et al* 1991). Any real object function contains null components for most imaging systems. Thus the knowledge of the null functions can quantify the components of an object that cannot be intrinsically measured by the imaging system.

Consider a PC system that images an object $f(\boldsymbol{r})$ lying in an infinite-dimensional Hilbert space, where $\boldsymbol{r}$ is a vector with p components lying in $\mathbb{R}^p$. The PC system records the number of counts in a finite number of bins, say M, so that the acquired image $\boldsymbol{g}$ is an M-dimensional vector lying in the Euclidean vector space $\mathbb{E}^M$. The PC system operator $\mathcal{H}$ thus maps from the set of functions lying in the infinite-dimensional Hilbert space $\mathbb{L}_2(\mathbb{R}^p)$ to the set of vectors lying in the finite-dimensional vector space $\mathbb{E}^M$. This mapping has an infinite-dimensional null space due to dimensionality considerations. Thus, there is an infinite set of null functions f_{null}, such that $\mathcal{H}f_{\text{null}} = 0$. Alternatively, there is an infinite set of object features that cannot be measured by the PC systems. The presence of these null functions could cause an infinite bias in a parameter estimated from the image data. For example, it is well known that the value inside a voxel, or any binary region of interest (ROI) that abruptly demarcates the signal from the background, is fundamentally not estimable using PC systems since such an ROI consists of high-frequency features, which almost always lie in the null space of PC systems (Kupinski *et al* 2013).

In contrast, consider a PP system imaging the same object $f(\boldsymbol{r})$. The PP system estimates q attributes per detected photon, where these attributes lie in a continuous space. Thus, the PP system operator $\mathcal{L}$, as discussed in section 2.1, maps from from the set of functions $f(\boldsymbol{r})$ that lie in $\mathbb{L}_2(\mathbb{R}^p)$ to the set of functions that lie in $\mathbb{L}_2(\mathbb{R}^q)$. While this system could have a null space, if $q \geqslant p$, the null space is not demanded by dimensionality considerations. Thus it is possible that PP systems could potentially measure a larger set of object features and provide a platform to overcome several issues in estimability that are otherwise present in PC systems.

We can compute the null functions from the pseudoinverse of the imaging system operator. Considering an object $f(\boldsymbol{r})$ being measured by a PP system described by the system operator $\mathcal{L}$, the measured component of this object is given by Barrett and Myers (2004)

$$f_{\text{meas}}(\boldsymbol{r}) = [\mathcal{L}^+ \bar{u}](\boldsymbol{r}). \tag{56}$$

Thus, using equation (54), the null component of this system is given by

$$f_{\text{null}}(\boldsymbol{r}) = f(\boldsymbol{r}) - f_{\text{meas}}(\boldsymbol{r}) \tag{57}$$

Using the expressions derived in equations (32) and (53), we can obtain the null functions for the 2D planar and 2D SPECT PP imaging systems, respectively.

In this paper, we will compare the null functions for the 2D PP SPECT system and the corresponding PC system. The PC system bins the position of interaction and the angular orientation attribute into a certain number of bins. To ensure a fair comparison, we must estimate the continuous null functions for this PC system. For this purpose, we have derived a method to determine the discrete-continuous pseudoinverse of the PC system operator in the absence of the estimation blur. The procedure to compute the pseudoinverse is presented in the appendix A. The continuous null functions for PC systems are computed from the pseudoinverse using equations analogous to equation (56) and (57) for PC systems.

3.2. Designing an analytic reconstruction algorithm

While there has not been previous research on reconstruction with PP systems, there are quite a few methods available to reconstruct with LM data (Parra and Barrett 1998, Bouwens *et al* 2001, Reader *et al* 2002, Khurd and Gindi 2004, Defrise *et al* 2005, Reader and Zaidi 2007, Schretter 2009). However, these methods assume that the object is a discrete vector, and, since objects are continuous functions, this can lead to information loss. For example, let us consider an object function $f(\boldsymbol{r})$ that lies in the infinite-dimensional Hilbert space $\mathbb{L}_2(\mathbb{R}^p)$. The general form of a linear approximation to this object function in a discrete basis is given by

$$f_a(\boldsymbol{r}) = \sum_{n=1}^{N} \alpha_n \psi_n(\boldsymbol{r}), \tag{58}$$

where the subscript *a* denotes approximate and $\{\psi_n(\boldsymbol{r}), n = 1, 2, \ldots, N\}$ denote a convenient set of expansion functions. Thus, under this representation, the object is approximated by the vector $\boldsymbol{\alpha} = \{\alpha_1, \alpha_2, \ldots \alpha_n\}$, which lies in the finite-dimensional Euclidean space $\mathbb{E}^N$. Existing reconstruction algorithms for LM data assume that the object is represented as this discrete vector $\boldsymbol{\alpha}$, and estimate the elements of this vector. Thus, the solution obtained with these algorithms is an estimate of $\boldsymbol{\alpha}$, which only provides an approximation to the object function $f(\boldsymbol{r})$. Further, parameters of the object estimated from the coefficients $\boldsymbol{\alpha}$ can potentially be biased due to the null functions of the expansion functions ψ_n with respect to the imaging system (Kupinski *et al* 2013).

These sources of information loss can be avoided by not making the assumption that the object is a discrete vector and estimating a continuous object function from the LM data. In this context, PP systems present us with the advantage that they yield data defined on a continuous domain. Thus an analytical technique could be designed that estimates a continuous object function from the continuous LM data by exploiting the CC formalism of the LM operator. One such possible technique is to apply the CC pseudoinverse of the LM operator on the noisy LM data, i.e.

$$\hat{f}(\boldsymbol{r}) = [\mathcal{L}^+ \boldsymbol{u}](\boldsymbol{r}). \tag{59}$$

This approach yields a minimum-norm least squares estimate of the continuous object function (Barrett and Myers 2004). Note that since the LM operator relates the LM data to the continuous object function, this approach does not assume that the object is a discrete vector. In the noise-free case, it can be shown that $\hat{f}_{\mathrm{nfree}}(\boldsymbol{r}) = [\mathcal{L}^+ \boldsymbol{u}](\boldsymbol{r})$. Since the $\mathcal{L}$ operator is linear, equation (59) will lead to the noise-free solution in a mean sense, i.e. $\langle \hat{f}(\boldsymbol{r}) \rangle_{\boldsymbol{u}|f} = \hat{f}_{\mathrm{nfree}}(\boldsymbol{r})$, where $\langle \ldots \rangle$ denotes the mean of the quantity inside the parenthesis.

Considering the 2D SPECT system as described in section 2.4 and substituting the expression for the pseudoinverse for the LM operator for this system (equation (53)) in equation (59), an estimate for the object function $\hat{f}(\boldsymbol{r})$ is given by

$$\hat{f}(\boldsymbol{r}) = \frac{\pi}{\tau} \int_0^\pi \mathrm{d}\theta \int_{-\infty}^\infty \mathrm{d}\hat{p} \int_{-\infty}^\infty \mathrm{d}\rho \ |\rho| \exp[2\pi \mathrm{i}\rho(\boldsymbol{r} \cdot \hat{\boldsymbol{n}}_\theta - \hat{p})] \exp(2\pi^2 \sigma_p^2 \rho^2) u(\hat{p}, \theta), \tag{60}$$

where we have replaced $r_1(\theta)$ by $\boldsymbol{r} \cdot \hat{\boldsymbol{n}}_\theta$. Substituting the expression for $u(\hat{p}, \theta)$ from equation (33), and using the sifting property of the delta function, we obtain

$$\hat{f}(\boldsymbol{r}) = \frac{\pi}{\tau} \sum_{j=1}^J \int_{-\infty}^\infty \mathrm{d}\rho \ |\rho| \exp[2\pi \mathrm{i}\rho(\boldsymbol{r} \cdot \hat{\boldsymbol{n}}_{\theta_j} - \hat{p}_j)] \exp(2\pi^2 \sigma_p^2 \rho^2)$$

$$= \frac{\pi}{\tau} \sum_{j=1}^J [\mathcal{F}^{-1}\{|\rho| \exp(2\pi^2 \sigma_p^2 \rho^2)\}](\boldsymbol{r} \cdot \hat{\boldsymbol{n}}_{\theta_j} - \hat{p}_j), \tag{61}$$

where $\mathcal{F}^{-1}$ denotes the 1D inverse Fourier transform operator. While the above expression does yield an estimate of the object function, the solution is very sensitive to noise. The noise components at the high frequency are amplified because the value of the reciprocal of the Gaussian function, i.e. $\exp(2\pi^2 \sigma_p^2 \rho^2)$, increases rapidly with frequency. To resolve this issue, we require a filter that can suppress the effect of noise at high frequencies; we use a Metz filter for this purpose King *et al* (1984). The Fourier transform of the estimation blur, i.e. the Gaussian function, is the modulation transfer function (MTF) of the imaging system, i.e.

$$\mathrm{MTF}(\rho) = \exp(-2\pi^2 \sigma_p^2 \rho^2). \tag{62}$$

The Metz filter is given by

$$M(\rho) = \frac{1}{\mathrm{MTF}(\rho)} [1 - \{1 - \mathrm{MTF}(\rho)^2\}^X]. \tag{63}$$

This filter is made up of two terms, the inverse of the MTF, and a low-pass filter that suppresses the effect of noise at high frequencies. The magnitude of X determines when the low-pass filter begins to dominate. The expression for the estimate of the object function after incorporating this filter is given by

$$\hat{f}(\boldsymbol{r}) = \frac{\pi}{\tau} \sum_{j=1}^J [\mathcal{F}^{-1}\{|\rho| M(\rho)\}](\boldsymbol{r} \cdot \hat{\boldsymbol{n}}_{\theta_j} - \hat{p}_j). \tag{64}$$

Thus, the reconstruction is equivalent to filtering each LM event, shifting the filtered output by a value equal to the position of interaction of the LM event and back-projecting the result into object space at an angle given by the angular orientation at which the LM data was acquired. This algorithm is not guaranteed to yield positive values for $f(\boldsymbol{r})$. Since the activity distribution is non-negative valued for all $\boldsymbol{r}$, we apply a positivity constraint on the estimated object function. An analytical reconstruction algorithm is thus obtained for the 2D SPECT system. A similar analytic reconstruction algorithm can be derived for the 2D planar LSIV system.

4. Methods

To compute the null functions and study the performance of the proposed reconstruction method, we performed several experiments. These experiments involved generating noise-free

and noisy data for PP and PC systems and implementing and evaluating the efficacy of the proposed reconstruction algorithm. For the experiments, we used the 2D SPECT system described in section 2.4.

4.1. Simulating the PP system

4.1.1. Generating noise-free data. To obtain the noise-free data $\bar{u}(\hat{p}, \theta)$ from the 2D PP SPECT system, in accordance with equation (3), we should apply the CC operator $\mathcal{L}$, whose kernel is given by equation (40), on an object function $f(\boldsymbol{r})$. An appropriate method to generate this noise-free data is to consider an object function that can be expressed analytically, and then use it to derive a mathematical expression for $\bar{u}(\hat{p}, \theta)$. From equation (40), the analytic derivation of $\bar{u}(\hat{p}, \theta)$ consists of two steps: (a) Take the Radon transform of the object, and (b) Convolve the computed Radon transform with a 1D Gaussian kernel of variance σ_p^2 to model the estimation blur. We chose the Shepp–Logan phantom (Shepp and Logan 1974) as the continuous object function, since it could be expressed analytically and we could mathematically derive an expression for the Radon transform for this object function. As mentioned previously, the derived pseudoinverse of the PC system operator did not account for the process of estimating the photon attributes. Thus, to ensure a fair comparison, we ignored the estimation blur in both the PP and PC systems.

Since the simulation was on a digital platform, we were restricted to calculate the value of $\bar{u}(\hat{p}, \theta)$ only at a finite set of values for $\hat{p}$ and θ. We chose these values to be finely spaced, so that the computed values would replicate the data obtained over an almost continuous domain. In our experiments, the detector length and the angular range of the detector were 2 units and π radians, respectively. We evaluated the values of $\bar{u}(\hat{p}, \theta)$ for 512 equally spaced values of both $\hat{p}$ and θ.

To investigate the null functions of PP and PC systems for an object function with many high frequency features, we also considered another object function that consisted of several horizontal and vertical edges. This object function, as presented in figure 3(a), consisted of 2D rect functions of different sizes, and the difference of two 2D rect functions that resulted in a rectangular border with no activity in the interior. The Radon transform of the continuous version of this object was difficult to compute. Thus, this object was instead defined as a discrete vector over a very finely spaced grid. Note that due to the shape of this object, it could be represented accurately, without any approximations, in this grid. Next, the Radon transform was numerically computed for finely spaced values of p and θ. The rest of the procedure to obtain the noise-free data was the same as for the Shepp–Logan phantom.

4.1.2. Generating noisy data. To generate the noisy data from the PP system, we first determined the number of LM events by sampling a Poisson distribution with a mean given by the total activity in the object. The object function was again chosen to be the Shepp–Logan phantom. Since we ignored attenuation and scatter in this analysis, the probability of detection at each angle was constant. Thus, for the jth LM event, the angular orientation of the detector θ_j was determined by sampling a uniform distribution of angle values between 0 and π radians. To determine the position of interaction p_j of this LM event, we used the Radon transform to analytically determine the projection data from the continuous object function at the projection angle θ_j. We treated this projection data as the probability density function (PDF) of p_j, and sampled this PDF to determine p_j. To perform this step numerically, the projection data were computed for 512 equally spaced values of the position of interaction, yielding a binned representation of the the PDF of p_j, i.e. a histogram, of p_j. Then, using the inverse-transform

sampling scheme (Papoulis and Pillai 2002), we sampled this histogram to determine the bin to which p_j would belong. Uniformly sampling a location within this bin yielded p_j. Note that p_j was a continuous random variable, and not binned in any way, even though we generated it on a computer. To account for estimation blur, we then sampled another Gaussian distribution with mean equal to the true position of interaction, and variance equal to the variance of the estimation blur. We thus obtained the estimated position of interaction $\hat{p}_j$ for the LM event. This yielded the noisy PP system data.

4.2. GPU-based implementation of the reconstruction algorithm

In this section, we describe the GPU-based implementation of the reconstruction algorithm derived in section 3.2 for the 2D SPECT system. The proposed algorithm (equation (64)) estimates the continuous object function at any location. However, in our implementation, for display purposes, we evaluated the reconstructed object over a discrete pixel grid, where the size of the pixel could be arbitrarily small. We discretized the 2D reconstructed object space into pixels. For the ith pixel, we computed the value of $\hat{f}(r)$ at the center of the pixel. Thus, denoting the center of the ith pixel by the vector r_i and using equation (64), for each pixel we computed

$$\hat{f}(r_i) = \frac{\pi}{\tau} \sum_{j=1}^{J} [\mathcal{F}^{-1}\{|\rho| M(\rho)\}](r_i \cdot \hat{n}_{\theta_j} - \hat{p}_j). \tag{65}$$

This reconstruction scheme is parallelizable since we could evaluate the value of $\hat{f}(r_i)$ independently for all the pixels. We developed reconstruction code that was executed on a 2.1 GHz Intel Xeon E5-2620 system containing one NVIDIA Tesla K40m GPU card. The software was developed in C, and we used the Compute Unified Device Architecture (CUDA) C programming language (NVIDIA CUDA 2015, Jha *et al* 2012) to program the GPU hardware. The software first reads the input LM data and stores them in array format. The inverse Fourier transform of the function $|\rho| M(\rho)$ is next evaluated and stored in another array. Both these arrays are then transferred to the global memory of the GPU. We then invoke the CUDA kernels in parallel for each pixel, where in each CUDA kernel, the value of $f(r)$ at the center of the particular pixel is computed using equation (65). The computed output image is then transferred back to the main memory of the system. Finally, we apply a positivity constraint by setting the activity values of all the image pixels that have negative activity values to zero.

The proposed reconstruction algorithm has one regularization parameter, the order of the Metz filter X. To determine a suitable value for this parameter, we visually analyzed the reconstruction results for several values of X. We observed that $X = 1.5$ yielded results with good visual image quality. On increasing the filter order, the resolution of the reconstructed images was lowered, while choosing a lower value of X made the reconstructions look noisy. Based on this empirical study, we chose the value of X to be 1.5.

4.3. Reconstruction approach for PC systems

The main objective of the reconstruction-related experiments was to study the performance of the proposed reconstruction method for systems with finite object support, as is the case with real imaging systems. However, we also compared the reconstruction results obtained with PP systems that use the proposed reconstruction algorithm and PC systems that use an analogous reconstruction approach. The comparisons were meant to study whether PP systems can help overcome the artifacts that are introduced due to the binning of attributes in PC systems.
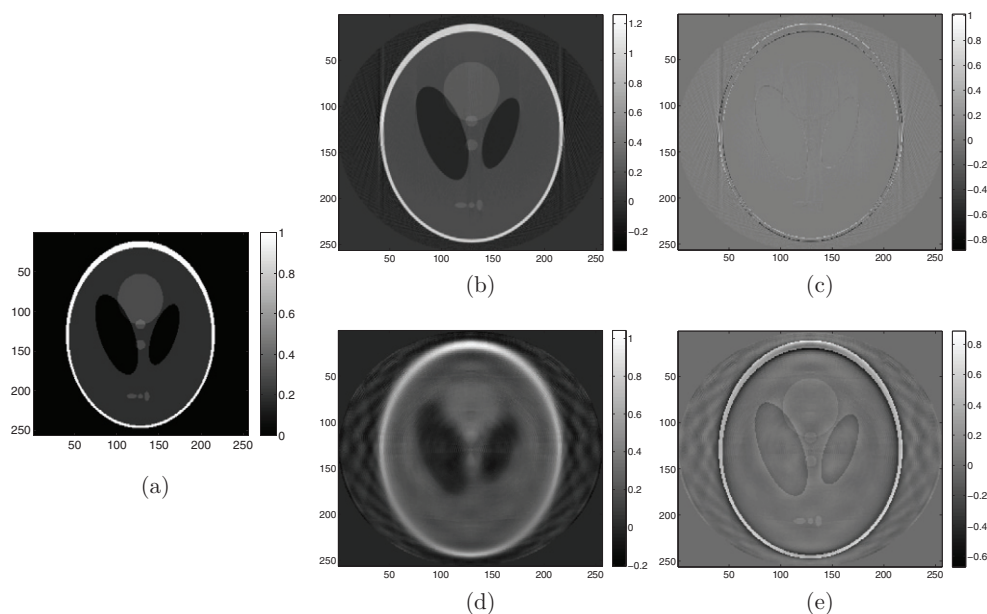
Figure 2. (a) The object function. (b) The measurement and (c) the null component for this object with the PP system. (d) The measurement and (e) the null components with the PC system.

The considered PC system binned the position and angular orientation attributes of the PP system into 128 spatial and 16 projection bins, respectively. The reason for choosing a lower number of projection bins was to visually demonstrate the artifacts that arise due to binning in PC systems, and investigate if PP systems can help overcome these artifacts. For the PC system, we used the filtered back-projection (FBP) algorithm to reconstruct the object. The FBP algorithm was chosen since it is often used to reconstruct object vectors with PC systems. Further, it is similar, and in many ways analogous to the proposed reconstruction approach for PP systems, since both the approaches are non-iterative and designed for 2D SPECT systems with ideal parallel-hole collimators. The FBP method was implemented in conjunction with the Metz filter (King *et al* 1984), where we chose the filter order to be 1.5, again based on empirical observations.

We note that neither the proposed SVD-based reconstruction algorithm nor the FBP algorithm were optimized using objective evaluation methods. Further, in the experiments, we did not objectively evaluate these algorithms. The experiments are mainly to give the reader a subjective idea of the performance of the SVD-based algorithm for PP systems and visually compare it with an empirically optimized FBP algorithm for PC systems. Thus, from these experiments, we do not draw any definitive conclusions comparing the proposed SVD-based algorithm and the FBP algorithm.

5. Results

5.1. Null functions with PP and PC systems

The computed null functions for the Shepp–Logan phantom with the PP and PC systems using the approach mentioned in section 3.1 are shown in figure 2. It is observed the PP system had
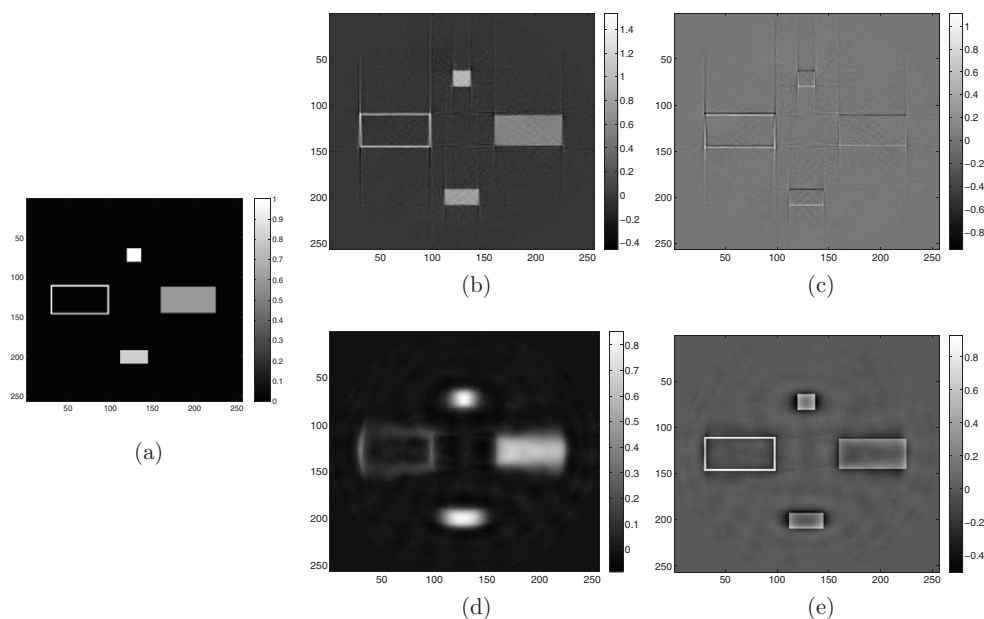
Figure 3. (a) The object function. (b) The measurement and (c) the null components for this object for the PP system. (d) The measurement and (e) the null component with the PC system.

a larger number of features in the measurement space as compared to the PC system. For example, the edges lay in the null space for the PC systems, but were present in the measurement space of the PP systems.

The null functions for the phantom are presented in figure 3(b) for the PP and PC SPECT system. We again observe that the high-frequency features, i.e. the edges, lay in the null space of the PC systems but were in the measurement space of the PP systems. This observation is best demonstrated by the presence of the thin-edge rectangular ring in the measurement space of the PP system and null space of the PC system.

5.2. Performance of the reconstruction algorithm

5.2.1. Varying the number of LM events. We first studied the performance of the proposed reconstruction algorithm as a function of the number of LM events. We varied the number of LM events from 1 million to 100 million. The standard deviation of the blur in the position estimate, σ_p, was set to half of the width of the position bin in the PC system. The results from this experiment are presented in figure 4. It is observed that for a low number of LM events, the reconstructed images had noise artifacts. As the number of LM events increased, the artifacts decreased and the reconstructed images had good visual quality. It is also visually observed that the object reconstructed with PP systems measured more object features and had lesser aliasing artifacts compared to those reconstructed with PC systems for all the count levels. Thus, even in the presence of noise, PP systems offered improved performance compared to the considered PC system. To demonstrate this further, we also plotted the linear profile of the true object function and the images reconstructed using the PP and PC systems. The linear profiles show that images reconstructed from the PP systems had better resolution than those reconstructed from the PC system at all count levels. The reconstruction result
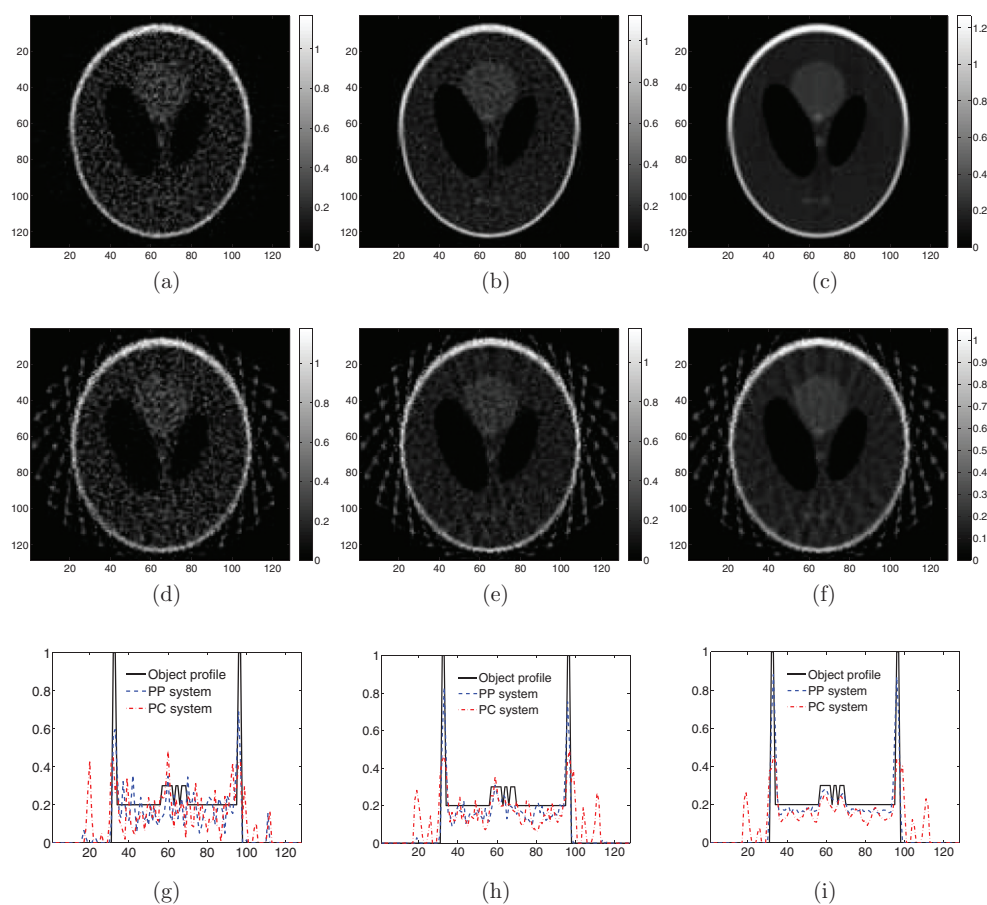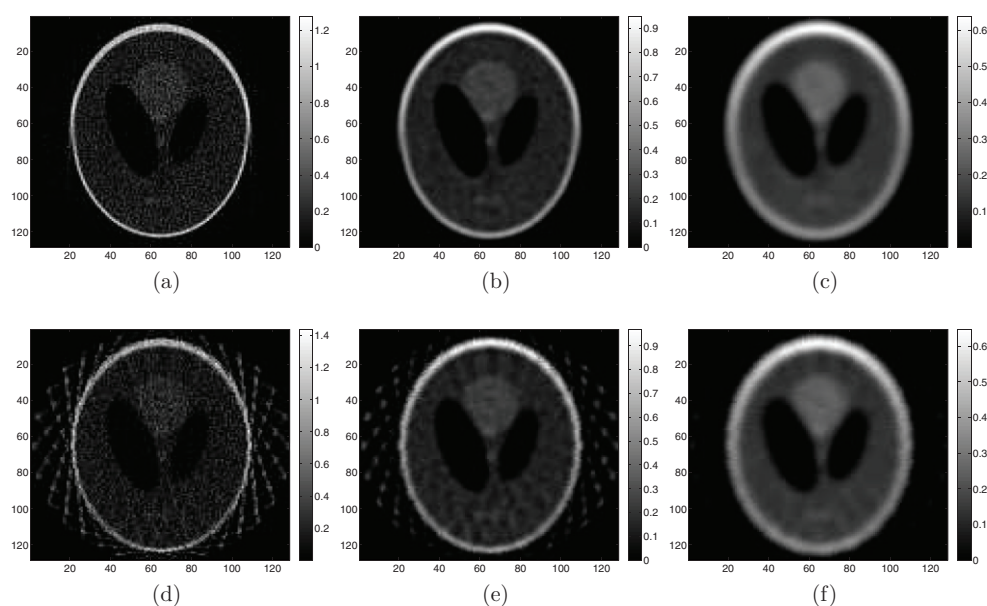
Figure 4. Reconstruction of the Shepp–Logan phantom using the proposed SVD-based reconstruction method for a PP SPECT system using: (a) 1 million; (b) 5 million; and (c) 100 million counts. (d)–(f) The reconstruction with the PC system for the same number of counts. A comparison of the linear profile of the reconstructed images is shown in figures (g)–(i).

with 100 million events especially helps to demonstrate that given a large number of events, excellent resolution could be achieved with PP systems. Further, this resolution could never be possible with PC systems due to their intrinsic limitation of an infinite-dimensional null space that would lead to aliasing artifacts.

5.2.2. Varying the standard deviation of the estimation blur.   In the next experiment, the standard deviation of the estimation blur was varied from 0.1 to 2 times the size of the position bin in the analogous PC system. We fixed the number of LM events to 5 million. The results presented in figure 5 show that on increasing the standard deviation of the blur, the resolution of the reconstructed object function degraded for both the PP and PC systems. Visually, the proposed reconstruction algorithm for the PP system yielded images with lesser artifacts compared to the FBP-based reconstruction algorithm for PC systems. The improved performance with the PP systems again shows that PP systems can help overcome the effects of angular aliasing even with noisy data.

Figure 5. Reconstruction of the Shepp–Logan phantom using the proposed SVD-based reconstruction method for a PP SPECT system with an estimation blur of (a) 0.5; (b) 1; and (c) 2 times the size of the detector bin width of the PC system. (d)–(f) The reconstruction with the PC system using the FBP-based approach with similar settings.

6. Discussions and conclusions

In this paper, we derived the SVD of the LM operator that describes PP nuclear imaging systems. We derived the SVD for two PP systems: a planar LSIV system, and a 2D SPECT system. We then used this SVD to compute the null functions for PP nuclear imaging systems. We also derived a technique to compute the null functions for PC SPECT systems. We showed that for the Shepp–Logan phantom and a phantom consisting of several high-frequency edges, the PP system had a smaller set of null functions in comparison to an analogous PC system.

We also designed an SVD-based reconstruction algorithm for PP systems and developed GPU-based code to implement this algorithm for the 2D PP SPECT imaging system. The algorithm was applied to reconstruct a continuous Shepp–Logan phantom object imaged by a simulated 2D SPECT system with finite object support. The proposed algorithm reconstructed images with good visual quality for these systems. We also compared the reconstruction results to results obtained using an FBP-based reconstruction algorithm with PC systems. The results demonstrated that in conjunction with the SVD-based approach, PP systems provide a platform to overcome the effects arising due to binning in PC systems even with noisy data.

In a PP system, we can also reconstruct the object on an event-by-event basis as the data is being acquired. We have developed another GPU-based software for this purpose. The execution time for this implementation is slightly longer, since the kernel is invoked for every LM event. For example, if the acquired data consists of about 10 million LM events and we reconstruct the object on a 128×128 pixel grid, processing all the LM events together takes about 11 s, but processing them on an event-by-event basis takes about 80 s. Thus, while the implementation that processes all the events together is preferable, for applications that require real-time reconstruction, the event-by-event version of the software could be used.

In our analysis, we evaluated the SVD for a continuously rotating 2D SPECT system with infinite object support. We can also use the proposed techniques to derive the SVD of a 2D SPECT system that has infinite object support and acquires data at discrete angles (Jha *et al* 2013). However, the expression for the pseudoinverse for this system computed using the SVD contains a mathematically undefined term. This could be because of the infinite object support, which leads to an infinite number of solutions for the reconstructed object. Limiting the analysis to an object with finite support might make the problem more tractable and we have made some initial investigations on this case (Jha 2013, Jha *et al* 2013).

The proposed analytic reconstruction method has several other applications apart from those mentioned in the introduction. The method offers a way to compare information-retrieval algorithms without being affected by the limitations of simulation studies, such as discretization and numerical precision. It also offer insights on the information content and information-retrieval capacity from the PP system data, which can help improve the design of the imaging system and the algorithm. For example, if the interest is in estimating a certain parameter from the data, then instead of applying the estimation algorithm on the reconstructed discrete object, we could instead directly apply it on the analytical reconstructed continuous object, and obtain a more accurate expression for the estimator. Also, the method can also provide insights into data sufficiency and sampling conditions. Further, an iterative algorithms often require significantly greater computation compared to one-step analytic methods. Thus, the proposed analytic algorithm could be especially useful when fast reconstructions are required, as in adaptive SPECT systems (Furenlid *et al* 2008).

The theoretical formalism that we have proposed can be extended to account for blur arising due to finite spatial resolution of the detector. The effective blur in that case can be expressed as a convolution of the estimation and PSF-related blurs. If the blur arising due to the finite spatial resolution of the detector is another Gaussian kernel, then we can express the blur due to the finite spatial resolution and estimation statistics as another Gaussian function with a variance equal to the sum of the variances of the two individual blurs. Also, while the proposed technique is for PP systems that perform ML estimation of the attributes, the technique could be adapted for systems that do not use an ML estimation procedure, if we can determine the PDF of the estimated attributes. If we cannot determine the PDF, a useful approximation results by assuming that the estimated value of the attribute is the same as the true value. In this case $\mathrm{pr}(\hat{A}|A)$ simply becomes a delta function, given by $\delta(\hat{A} - A)$, and all the above-derived formulas are valid in the limit of the variance of the estimated attribute tending to 0. There are many advantages to storing and processing data acquired in LM format even if the ML processing step is not involved, as described in Barrett *et al* (1997). The proposed method provides an avenue to reconstruct the object functions directly from the LM data for systems that store data in LM format.

Acknowledgments

Appendix

Consider the continuously rotating 2D SPECT system described in section 2.4, which, following data acquisition, bins the position and angular coordinates into a finite number of bins.

This system is described by a continuous-discrete (CD) operator, which we denote by $\mathcal{H}$. To find the pseudo-inverse of this operator, denoted by $\mathcal{H}^+$, we begin with the identity (Barrett and Myers 2004)

$$\mathcal{H}^+ = \mathcal{H}^\dagger [\mathcal{H}\mathcal{H}^\dagger]^+. \tag{A.1}$$

If $f(\mathbf{r})$ were to denote the object, then the radiance measured at a distance p from the detector center when the detector is aligned at an angle θ, which we denote by $\chi(\theta, p)$, is given by the Radon transform of the function $f(\mathbf{r})$, i.e.

$$\chi(p, \theta) = [\mathcal{R}f](p, \theta) = \int_\infty \mathrm{d}^2 r f(\mathbf{r})\delta(p - \mathbf{r}\cdot\hat{\mathbf{n}}_\theta), \tag{A.2}$$

where $\hat{\mathbf{n}}_\theta$ denotes a unit vector parallel to the detector surface when the detector is aligned at the angle θ, and where $\mathcal{R}$ denotes the Radon operator. Let the (m,k)th measurement be obtained by binning the spatial and angular coordinates from $p_m - \Delta p$ to p_m and $\theta_k - \Delta\theta$ to θ_n, respectively. We denote this measurement by $g_{m,k}$, where m and k index the binned position and angular orientation, respectively. Denoting the binning operator by $\mathcal{D}$, the output of the tomographic system is given by

$$g_{m,k} = [\mathcal{H}f]_{m,k} = [\mathcal{D}\mathcal{R}f]_{m,k} = \int_{\theta_k-\Delta\theta}^{\theta_k} \mathrm{d}\theta \int_{p_m-\Delta p}^{p_m} \mathrm{d}p \int_\infty \mathrm{d}^2 r \, f(\mathbf{r})\delta(p - \mathbf{r}\cdot\hat{\mathbf{n}}_\theta)$$

$$= \int_{\theta_k-\Delta\theta}^{\theta_k} \mathrm{d}\theta \int_\infty \mathrm{d}p \int_\infty \mathrm{d}^2 r \, f(\mathbf{r})\delta(p - \mathbf{r}\cdot\hat{\mathbf{n}}_\theta)[u(p - p_m) - u(p - p_m + \Delta p)], \tag{A.3}$$

where $u(x)$ denotes the Heaviside step function. Further using the sifting property of the delta function,

$$g_{m,k} = \int_{\theta_k-\Delta\theta}^{\theta_k} \mathrm{d}\theta \int_\infty \mathrm{d}^2 r \, f(\mathbf{r})[u(\mathbf{r}\cdot\hat{\mathbf{n}}_\theta - p_m) - u(\mathbf{r}\cdot\hat{\mathbf{n}}_\theta - p_m + \Delta p)]. \tag{A.4}$$

To obtain an expression for the $\mathcal{H}^\dagger$ operator, we write it as

$$\mathcal{H}^\dagger = \mathcal{R}^\dagger \mathcal{D}^\dagger, \tag{A.5}$$

where $\mathcal{R}^\dagger$ and $\mathcal{D}^\dagger$ denote the adjoint of the Radon and binning operators, respectively. The adjoint of the Radon transform is given by

$$[\mathcal{R}^\dagger \chi](\mathbf{r}) = \int_0^\pi \mathrm{d}\theta \, \chi(\mathbf{r}\cdot\hat{\mathbf{n}}_\theta, \theta). \tag{A.6}$$

Likewise, the adjoint of the binning operator is given by

$$[\mathcal{D}^\dagger g](p, \theta) = \sum_{m,k} [u(\theta - \theta_k) - u(\theta - \theta_k + \Delta\theta)][u(p - p_m) - u(p - p_m + \Delta p)]. \tag{A.7}$$

Using equations (A.5)–(A.7), we obtain

$$[\mathcal{H}^\dagger g](\mathbf{r}) = \sum_{m,k} \int_{\theta_k-\Delta\theta}^{\theta_k} \mathrm{d}\theta \, [\{u(\mathbf{r}\cdot\hat{\mathbf{n}}_\theta - p_m) - u(\mathbf{r}\cdot\hat{\mathbf{n}}_\theta - p_m + \Delta p)\}]g_{mk}. \tag{A.8}$$

Thus, using equations (A.4) and (A.8), we get the $\{(m,k),(m',k')\}$ element of $\mathcal{H}\mathcal{H}^\dagger$ to be

$$[\mathcal{H}\mathcal{H}^\dagger]_{(m,k),(m',k')} = \int_{\theta_{k'}-\Delta\theta}^{\theta_{k'}} d\theta' \int_{\theta_k-\Delta\theta}^{\theta_k} d\theta \int_\infty d^2r[u(\boldsymbol{r}\cdot\hat{\boldsymbol{n}}_{\theta'}-p_{m'})-u(\boldsymbol{r}\cdot\hat{\boldsymbol{n}}_{\theta'}-p_{m'}+\Delta p)]$$

$$\times [u(\boldsymbol{r}\cdot\hat{\boldsymbol{n}}_\theta-p_m)-u(\boldsymbol{r}\cdot\hat{\boldsymbol{n}}_\theta-p_m+\Delta p)]. \tag{A.9}$$

We assume that the system has a circular object support and evaluate the integral over $\boldsymbol{r}$ only within this object support. The integrand over $\boldsymbol{r}$ represents the intersection of two strips of width Δp each, which have one of their sides normal to the detector aligned at angle θ and θ', respectively. Thus, when this intersection is completely within the object support, then denoting the width of the detector pixel by ϵ, the expression for the intersecting area is given by $\epsilon^2/|(\sin(\theta-\theta')|$ when $\theta \neq \theta'$. When $\theta = \theta'$, then if $m = m'$, then this area is approximately given by $2\epsilon\sqrt{R^2-p_m^2}$, and if $m \neq m'$, then the strips do not overlap. We evaluate the integral over θ and θ' numerically, and thus compute the elements of $\mathcal{H}\mathcal{H}^\dagger$. Since this matrix is square, we can find the inverse of this matrix. Further, using equation (A.8) in equation (A.1), we can obtain the discrete-continuous pseudoinverse of the $\mathcal{H}$ operator.

References

Aarsvold J N and Barrett H H 1996 Symmetries of single-slice multiple-pinhole tomographs *IEEE Nuclear Science Symp. Conf. Record* vol 3 pp 1673–7

Anger H O 1958 Scintillation camera *Rev. Sci. Instrum.* **29** 27–33

Barrett H H, Aarsvold J N and Roney T J 1991 Null functions and eigenfunctions: tools for the analysis of imaging systems *Prog. Clin. Biol. Res.* **363** 211–26

Barrett H H, White T and Parra L C 1997 List-mode likelihood *J. Opt. Soc. Am.* A **14** 2914–23

Barrett H H, Hunter W C, Miller B W, Moore S K, Chen Y and Furenlid L R 2009 Maximum-likelihood methods for processing signals from gamma-ray detectors *IEEE Trans. Nucl. Sci.* **56** 725

Barrett H H, Myers K J and Caucci L 2014 Radiance and photon noise: imaging in geometrical optics, physical optics, quantum optics, and radiology *Proc. SPIE* **9193** 919302

Barrett H H, Myers K J, Hoeschen C, Kupinski M A and Little M P 2015 Task-based measures of image quality and their relation to radiation dose and patient risk *Phys. Med. Biol.* **60** R1

Barrett H H and Myers K J 2004 *Foundations of Image Science* (New York: Wiley)

Bora V, Barrett H H, Jha A K and Clarkson E 2015 Impact of the Fano factor on position and energy estimation in scintillation detectors IEEE *Trans. Nucl. Sci.* **62** 42–56

Bouwens L, Van de Walle R, Gifford H, King M, Lemahieu I and Dierckx R A 2001 LMIRA: list-mode iterative reconstruction algorithm for SPECT *IEEE Trans. Nucl. Sci.* **48** 1364–70

Caucci L, Hunter W C, Furenlid L R and Barrett H H 2010 List-mode MLEM image reconstruction from 3D ML position estimates *IEEE Nuclear Science Symp. Conf. Record* pp 2643–7

Caucci L and Barrett H H 2012 Objective assessment of image quality. V. Photon-counting detectors and list-mode data *J. Opt. Soc. Am.* A **29** 1003–16

Clarkson E, Palit R and Kupinski M A 2010 SVD for imaging systems with discrete rotational symmetry *Opt. Express* **18** 25306–20

Davison M E and Grunbaum F A 1981 Tomographic reconstruction with arbitrary directions *Commun. Pure Appl. Math.* **34** 77–119

Defrise M, Casey M E, Michel C and Conti M 2005 Fourier rebinning of time-of-flight PET data *Phys. Med. Biol.* **50** 2749

Eskin J 1997 Semiconductor gamma-ray imaging detectors for nuclear medicine *PhD Thesis* University of Arizona, Tucson, AZ, USA

Eskin J, Barber H B and Marks D 1998 Signal-processing method for gamma-ray semiconductor sensor *US Patent Specification* 5825033 A

Furenlid L R, Wilson D W, Chen Y C, Kim H, Pietraski P J, Crawford M J and Barrett H H 2004 FastSPECT II: a second-generation high-resolution dynamic SPECT imager *IEEE Trans. Nucl. Sci.* **51** 631–5

Furenlid L R, Hesterman J Y and Barrett H H 2005 Real-time data acquisition and maximum-likelihood estimation for gamma cameras *IEEE NPSS Real Time Conf.*

Furenlid L R, Moore J W, Freed M, Kupinski M A, Clarkson E, Liu Z, Wilson D W, Woolfenden J M and Barrett H H 2008 Adaptive small-animal SPECT/CT *IEEE Int. Symp. on Biomedical Imaging* pp 1407–10

Gullberg G T and Zeng G L 1994 A reconstruction algorithm using singular value decomposition of a discrete representation of the exponential radon transform using natural pixels *IEEE Trans. Nucl. Sci.* **41** 2812–9

Halmos P R and Sunder V S 1978 *Bounded Integral Operators on L2 Spaces* (Berlin: Springer)

Hesterman J Y, Caucci L, Kupinski M A, Barrett H H and Furenlid L R 2010 Maximum-likelihood estimation with a contracting-grid search algorithm *IEEE Trans. Nucl. Sci.* **57** 1077–84

Jha A K 2013 Retrieving information from scattered photons in medical imaging *PhD Thesis* College of Optical Sciences, University of Arizona, Tucson, AZ, USA

Jha A K, Kupinski M A, Barrett H H, Clarkson E and Hartman J H 2012 Three-dimensional Neumann-series approach to model light transport in nonuniform media *J. Opt. Soc. Am.* A **29** 1885–99

Jha A K, Barrett H H, Clarkson E, Caucci L and Kupinski M A 2013 Analytic methods for list-mode reconstruction *12th Int. Meeting on Fully Three-Dimensional Image Reconstruction in Radiology and Nuclear Medicine*

Kadrmas D J, Frey E C and Tsui B M 1996 An SVD investigation of modeling scatter in multiple energy windows for improved SPECT images *IEEE Trans. Nucl. Sci.* **43** 2275–84

Khurd P and Gindi G 2004 A globally convergent regularized ordered-subset EM algorithm for list-mode reconstruction *IEEE Trans. Nucl. Sci.* **51** 719–25

King M A, Schwinger R B, Doherty P W and Penney B C 1984 Two-dimensional filtering of SPECT images using the Metz and Wiener filters *J. Nucl. Med.* **25** 1234–40

Kupinski M K, Clarkson E W and Barrett H H 2013 Scanning linear estimation: improvements over region of interest (ROI) methods *Phys. Med. Biol.* **58** 1283–301

Lehovich A 2005 List mode SPECT Reconstruction using empirical likelihood *PhD Thesis* College of Optical Sciences, University of Arizona, Tucson, AZ, USA

Madsen M T 2007 Recent advances in SPECT imaging *J. Nucl. Med.* **48** 661–72

Marks D G, Barber H B, Barrett H H, Tueller J and Woolfenden J M 1999 Improving performance of a CdZnTe imaging array by mapping the detector with gamma rays *Nucl. Instrum. Methods Phys. Res.* A **428** 102–12

Miller B W, Barrett H H, Furenlid L R, Barber H B and Hunter R J 2008 Recent advances in BazookaSPECT: real-time data processing and the development of a gamma-ray microscope *Nucl. Instrum. Methods Phys. Res.* A **591** 272–5

Miller B W, Barber H B, Furenlid L R, Moore S K and Barrett H H 2009a Progress in BazookaSPECT *Proc. SPIE* **7450** 74500C (PMC: 3033223)

Miller B W, Furenlid L R, Moore S K, Barber H B, Nagarkar V V and Barrett H H 2009b System integration of FastSPECT III, a dedicated SPECT rodent-brain imager based on BazookaSPECT detector technology *IEEE Nuclear Science Symp. Conf. Record* pp 4004–08 (doi: 10.1109/NSSMIC.2009.5401924)

Miller B W, Gregory S J, Fuller E S, Barrett H H, Barber H B and Furenlid L R 2014 The iQID camera: an ionizing-radiation quantum imaging detector *Nucl. Instrum. Methods Phys. Res.* A **767** 146–52

Moore S, Barrett H and Furenlid L 2012 ModPET: a compact PET system employing modular gamma cameras, maximum-likelihood event-parameter estimation, and list-mode ML-EM reconstruction *J. Nucl. Med. Meeting Abstr.* **53** 491

NVIDIA CUDA 2015 C programming guide version 7.0

Papoulis A and Pillai S U 2002 *Probability, Random Variables and Stochastic Processes* 4th edn (New Delhi: Tata McGraw-Hill)

Park S, Witten J M and Myers K J 2009 Singular vectors of a linear imaging system as efficient channels for the Bayesian ideal observer *IEEE Trans. Med. Imaging* **28** 657–68

Parra L and Barrett H H 1998 List-mode likelihood: EM algorithm and image quality estimation demonstrated on 2D PET *IEEE Trans. Med. Imaging* **17** 228–35

Paxman R G, Barrett H H, Smith W E and Milster T D 1985 Image reconstruction from coded data: II. Code design *J. Opt. Soc. Am.* A **2** 501–9

Peterson T E and Furenlid L R 2011 SPECT detectors: the Anger camera and beyond *Phys. Med. Biol.* **56** R145–82

Reader A J, Ally S, Bakatselos F, Manavaki R, Walledge R J, Jeavons A P, Julyan P J, Sha Z, Hastings D L and Zweit J 2002 One-pass list-mode EM algorithm for high-resolution 3D PET image reconstruction into large arrays *IEEE Trans. Nucl. Sci.* **49** 693–9

Reader A J and Zaidi H 2007 Advances in PET image reconstruction *PET Clin.* **2** 173–90

Schretter C 2009 Event-by-event image reconstruction from list-mode PET data *IEEE Trans. Image Process.* **18** 117–24

Shepp L A and Logan B F 1974 The Fourier reconstruction of a head section *IEEE Trans. Nucl. Sci.* **21** 21–43

Taguchi K and Iwanczyk J S 2013 Vision 20/20: single photon counting x-ray detectors in medical imaging *Med. Phys.* **40** 100901

Wilson D and Barrett H 1998 Decomposition of images and objects into measurement and null components *Opt. Express* **2** 254–60

Zeng G L and Gullberg G T 1997 An SVD study of truncated transmission data in SPECT *IEEE Trans. Nucl. Sci.* **44** 107–111